ACS Energy LETTERS

http://pubs.acs.org/journal/aelccp

PERSPECTIVE

X-ray Micro-Computed Tomography for Structural Analysis of All-Solid-State Battery at Pouch Cell Level

Published as part of ACS Energy Letters special issue "The Evolving Landscape of Energy Research: Views from the Editorial Team".

Chen-Jui Huang, Jin An Sam Oh, Marta Vicencio, Tianchen Hu, Hedi Yang, James N. Burrow, Yen-Fang Song, Gung-Chian Yin, Pavel Shevchenko, Kamila M. Wiaderek, Bing Joe Hwang, and Ying Shirley Meng*

Cite This: ACS Energy Lett. 2025, 10, 3459−3470

Read Online

ACCESS | Metrics & More | Article Recommendations | Supporting Information

ABSTRACT: Characterizing the microstructure of all-solid-state batteries (ASSBs) during fabrication and operation is vital for their advancement, particularly as scaling to pouch cell levels introduces challenges in probing large-scale microstructural evolution. This work highlights the potential of synchrotron X-ray micro-computed tomography (sXCT) as a nondestructive, rapid (<30 min), and high-resolution technique for visualizing and quantifying key microstructural features, including overhang, porosity, contact loss, active surface area, and tortuosity, in all-solid-state pouch cells. The large field of view (up to millimeters) of sXCT enables detailed analysis at an industry-relevant scale, bridging the gap between laboratory research and commercial applications. Furthermore, integrating realistic sXCT-derived 3D models into multiphysics simulations could provide insights into chemo-mechanical degradation, particularly at the edges of the pouch cells, offering a pathway for designing robust, high-performance ASSBs. This perspective establishes sXCT as an indispensable tool for advancing both the understanding and the engineering of next-generation energy storage systems.

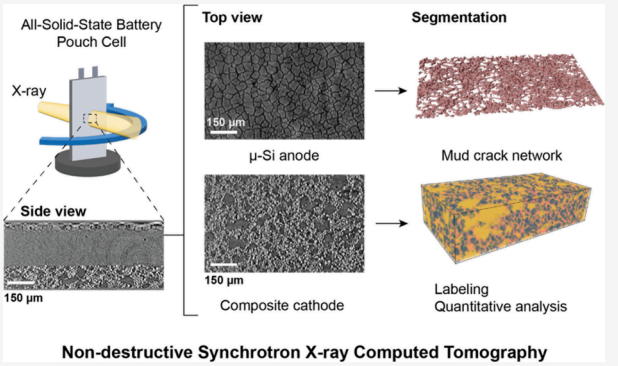

All-solid-state batteries (ASSBs) using intrinsically nonflammable solid-state electrolytes (SSEs) show promise as an alternative energy-dense storage solution due to their achievable higher energy density and improved safety.[1−4] In contrast to conventional lithium-ion batteries, which benefit from facile ion transport via infiltration of liquid electrolytes into porous electrodes, ASSBs require physical contact between solid materials to facilitate the electrochemical reactions. In an ideal scenario, all components in the ASSBs should exhibit fully densified microstructures that lack any porosity to maximize volumetric energy density. However, the mismatch in particle sizes and mechanical properties of materials induces unavoidable porosity or nonideal tortuosity within practical ASSBs. Either formed in the initial fabrication process or during the battery operation due to volume changes of cathode/anode materials, the pores and gaps in the microstructure can lead to contact loss and propagation of fractures/cracks.[5] Contact loss of active material (AM) reduces the utilization, thus leading to lower reversible capacity and capacity fading over time.[2] Meanwhile, voids and fracture formation within the microstructure could also lead to structural degradation[6,7] or cell failure[8,9] due to the disruption of ion percolation pathways.

Many researchers have sought to use computational simulations to better understand the ASSBs electrochemical performance and physical morphological changes. However, these studies used a hypothetical model that does not truly reflect on the actual tomography, which raises the reliability of such analysis. Thus, a large-scale tomography will improve our understanding of ASSBs, elevating the technology potential

Received: March 26, 2025
Revised: May 7, 2025
Accepted: May 27, 2025

commercially. To quantitatively investigate the internal microstructure and its evolution within ASSBs during fabrication and cycling, three-dimensional (3D) tomography and reconstruction techniques are essential. Figure 1 and Table 1 compare three different methods of 3D tomography using focused-ion beam-scanning electron microscopy (FIB-SEM), lab-based X-ray computed tomography (lab-XCT), and synchrotron XCT (sXCT). The cross-section images of a composite cathode electrode captured by FIB-SEM and sXCT can be found in Figure S1 for visual comparison.

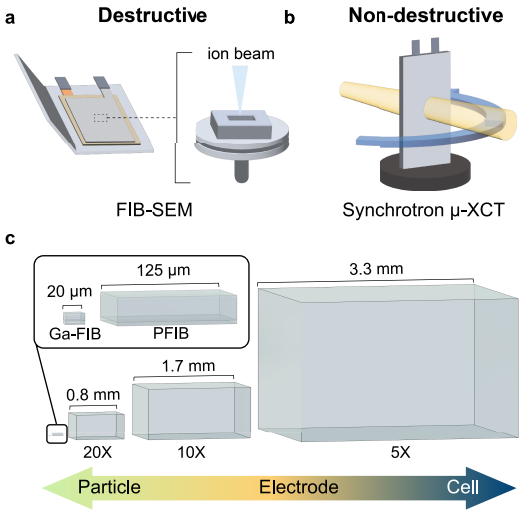

Figure 1. Comparison of 3D FIB-SEM and synchrotron μ-XCT. (a) Schematics showing the characterization condition of (a) 3D FIB-SEM and (b) synchrotron μ-XCT. (c) Field of view and the corresponding imaging component level of Ga-FIB, PFIB, and micro-XCT at different magnifications. The field of view used here refers to the μ-XCT beamline TPS-31A at Taiwan Photon Source, Taiwan.

3D FIB-SEM is often used to quantify battery microstructures, such as networks of microcracks and the carbon binder domains (CBD) within cathode electrodes[10] and the porosities of deposited Li-metal anodes,[11−13] with nanometer-scale resolution. However, the sample preparation process necessitates the disassembly of the battery and can induce unwanted artifacts that misrepresent the native state if the sample preparation/transfer process is not strictly controlled.[14] Depending on the focused ion beam sources, the field of view can be <50 μm using Ga^+ and up to ~100 μm when using Xe^+ plasma FIB-SEM (PFIB-SEM)[15] (Figure 1a). It is noteworthy that due to the formation of alloy with Li metal at room temperature, Ga^+-ion source is intrinsically incompatible with metallic Li-based samples unless in a cryogenic environment,[16] limiting the application of Ga^+-FIB-SEM for Li-ASSB studies.

Besides meticulous sample preparation, which is highly dependent on the operator's experiences and skills, 3D tomography using FIB-SEM is a time-consuming process, typically requires several hours, and such highly localized characterization (e.g., small field of view) can pose a challenge for acquiring statistically relevant data sets. Hence, while 3D FIB-SEM can provide a high spatial resolution, it is a destructive technique for 3D tomography, which limits it to *ex situ* observation (Figure 1a) and is unable to truly reflect the bulk microstructure of the battery components.

> X-ray computed tomography, as a noninvasive imaging technique allowing *in situ* and *operando* characterization, can probe the internal microstructure of ASSBs nondestructively without disassembling batteries.

XCT, as a noninvasive imaging technique allowing *in situ* and *operando* characterization, can probe the internal microstructure of ASSBs nondestructively without disassembling batteries (Figure 1b).[21] The technique can be categorized into either lab-based or synchrotron-based XCT, depending on the X-ray source. Although lab-XCT and sXCT share similar spatial resolution around 1 μm, the imaging time and quality are drastically different. For synchrotron-based monochromatic parallel beams, with at least 1000 times higher flux than the polychromatic cone-beam on the lab-XCT machines, the acquisition time for one tomogram can be down to seconds, which is significantly faster than lab-XCT.[21−25] Besides, the capability of tunable energy monochromatic X-ray beam for absorption contrast and phase contrast for light matter/boundaries show the unique and indispensable characteristics of sXCT that is superior to lab-XCT.[21,22] Lastly, it should be noted that nano-XCT is not discussed due a much smaller field of view (<100 μm), even though the imaging time can be achieved down to minutes, that lies outside the scope of this work focusing on capturing ASSB pouch cell bulk structure at micrometer level.

Critically, due to the nondestructive nature of sXCT, the ASSB pouch cells were imaged as is without any specific modification or preparation prior to the sXCT experiments. Although micro-sXCT has 1 order of magnitude lower spatial resolution compared to SEM at the submicron level, the imaging time for one tomogram is significantly shorter (generally within 30 min). Moreover, structural information from the particle (submicron) up to the cell level (millimeter) can be characterized with different magnification lenses (Figure 1c). The shorter imaging time and nondestructive nature of sXCT also enable real-time monitoring of the ASSB microstructural evolution through *in situ*/*operando* experiments

Table 1. Comparison of 3D Tomography Using (P)FIB-SEM and X-ray Micro-CT

	(P)FIB-SEM[10,15,17]	Lab μ-XCT[8,18,19]	Synchrotron μ-XCT[8,20,21]
Cell condition	Cell disassembled (destructive)	Cell intact (nondestructive)	Cell intact (nondestructive)
Highest spatial resolution	10−20 nm	~1 μm	~1 μm
Field of view	~10 to ~100 μm	~100 μm to ~10 cm	~100 μm to ~10 mm
Imaging time (one tomogram)	~hours	~hours	seconds to minutes
In situ/*operando*	×	√	√

https://doi.org/10.1021/acsenergylett.5c00956
ACS Energy Lett. 2025, 10, 3459−3470

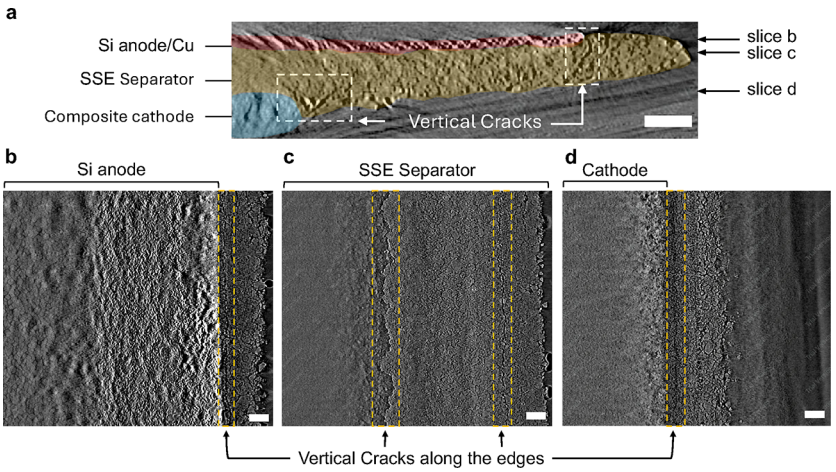

Figure 2. Top-down sXCT slice of ASSB pouch cell at edge region. (a) Cross-section sXCT slice of all-solid-state pouch cell showing cracks along electrode edges. The top-down xz slices of the cycled cell edge at the (b) Si anode, (c) SSE separator, and (d) cathode electrode plane. Scale bar: 200 μm.

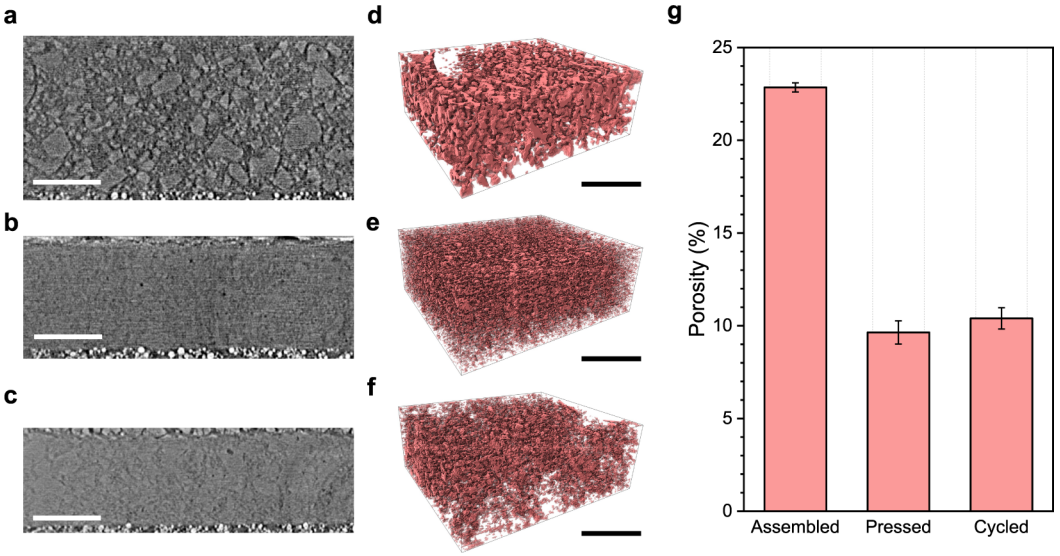

Figure 3. Microstructure and quantitative analysis of separator layer in pouch cell at different states: assembled, pressed, and cycled. The cross-section xy slice of (a) assembled, (b) pressed, and (c) cycled pouch cells showing separator layer and composite cathode. Scale bar: 100 μm. 3D model of pores in LPSCl separator of (d) assembled, (e) pressed, and (f) cycled pouch cells. Scale bar: 100 μm. (g) Bar chart showing the porosity of LPSCl separator in the assembled, pressed, and cycled pouch cells.

that are close or identical to the actual battery cycling environment/conditions.[7−9,26,27]

With the recent progression in ASSBs toward larger proof-of-concept cell formats, analyzing the bulk microstructure of individual components is essential for gaining deeper insights into their electrochemical performances. In this work, we probed the microstructure of the ASSBs by sXCT using absorption contrast imaging mode at beamline 31A, Taiwan Photon Source (Figure S2a,b). The analysis includes three stages: before cold isostatic pressing (CIP) at 500 MPa, referred to as "assembled"; after the CIP process, referred to as "pressed"; and post-C-rate test cycling at 5 MPa, referred to as "cycled". The cell dimensions, configuration, and schematics illustrating the visualized plane of sXCT slices are shown in Figure S3, while the electrochemical cycling data for the cycled pouch cell are provided in Figure S4. The sXCT images of the entire stacks of each cell are provided in Figure S5a-c.

It should be noted that the sXCT imaging was carried out without stack pressure applied to the cell, which might not have fully reflected realistic microstructure under the cycling pressure. Nevertheless, the porosity/contact surface area evolution trends showing the effect of CIP densification and gaps/voids formation after cycling provide microstructural insights that were not easily accessed by other characterization techniques. Future experiments will focus on tracking the microstructure evolution within the same cell *in situ* to understand these shifts better, allowing for more correlative and comparable quantitative analysis. The development of *in situ/operando* cell holders capable of applying stack pressure during sXCT imaging is currently underway and will be reported in future work. Finally, perspectives on leveraging the realistic 3D sXCT models for Multiphysics simulation are provided to further understand the chemo-mechanical degradation mechanisms of ASSBs.

https://doi.org/10.1021/acsenergylett.5c00956
ACS Energy Lett. 2025, 10, 3459−3470

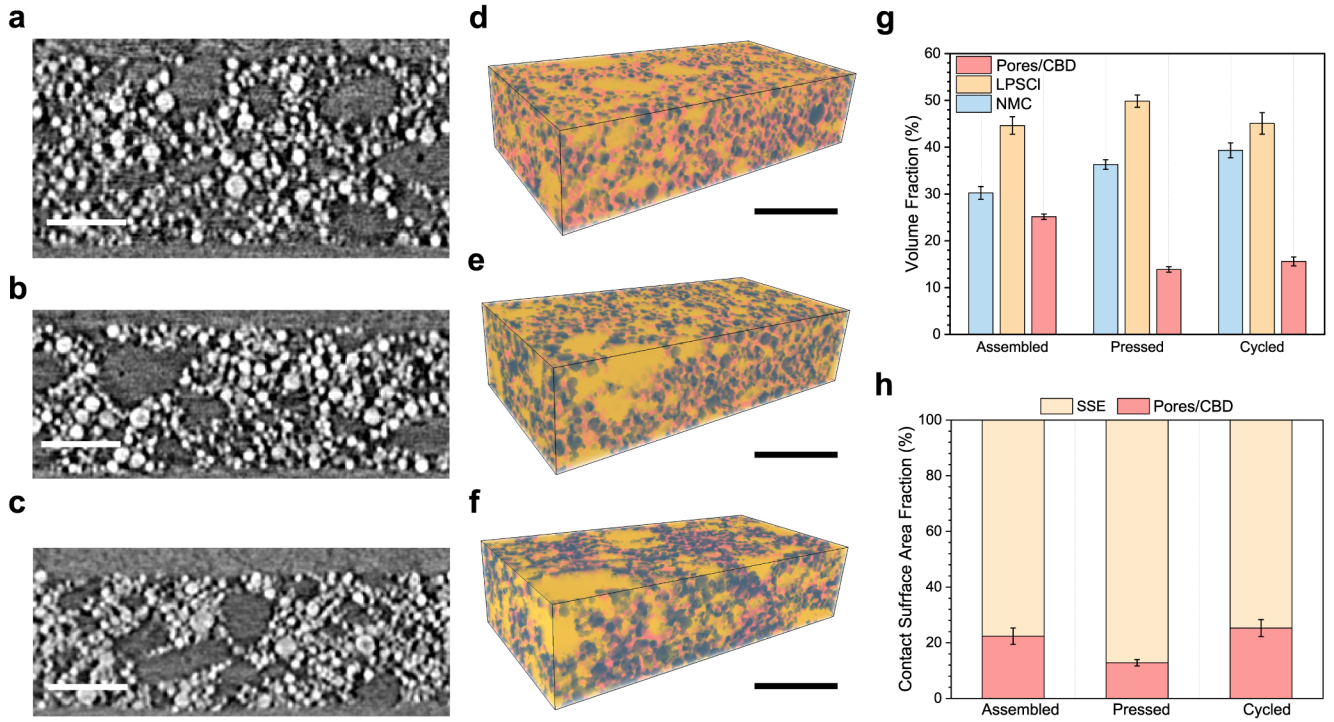

Figure 4. Microstructure and quantitative analysis of composite cathode in pouch cell at different states: assembled, pressed, and cycled. The cross-section xy slice of (a) assembled, (b) pressed, and (c) cycled pouch cells showing the composite cathode. Scale bar: 75 μm. 3D segmented model of (d) assembled, (e) pressed, and (f) cycled pouch cells. Scale bar: 100 μm. In the 3D models, SSE is shown in yellow, NMC811 in blue, and pores/CBD in light red. (g) Volume fraction of each component within the composite cathode in different samples. (h) Contact surface area fraction of cathode active material in the cathode composite electrode.

MACROSTRUCTURE DEFECTS

Densification of inorganic compounds typically leads to increased brittleness of the layer as there is a limited stress relief mechanism in the ASSBs.[28] Furthermore, thin inorganic SSE separators with limited strength are more prone to fracture due to any external/internal forces. Thus, densification of components is commonly the final step in pouch cell fabrication. With a larger field of view, sXCT visualizes the edges of the components in the cell from cross-section (Figure 2a) and top-down (Figure 2b-d) at millimeter scales. Although the LPSCl separator remained largely intact, vertical cracks were observed along the edges of both cathode and anode. This likely stems from the accumulation of stress at the electrode edges due to the mismatched dimension of the layers, which is necessary to ensure proper cycling of batteries,[29−32] inducing localized stress or pivot for bending. Consequently, any inhomogeneous forces during processing, handling, or operation can lead to vertical fractures that propagate into the highly brittle SSE layer.

The vertical fractures are highly undesirable for lithium metal-based ASSBs as they can act as the propagation pathways for Li dendrite creeping, leading to cell short-circuiting. Meanwhile, crediting the nondestructive imaging approach, we confirmed that the defective ASSB analyzed here still exhibits electrochemical activity. This could be attributed to the silicon anode used in this work, serving as a lithium-ion host, and having a higher tolerance for such defects. Notably, this is the first report of such defects in ASSBs, which are challenging to image using FIB-SEM due to limited field of view. This observation exemplifies sXCT's advantage of visualizing microstructural defects of ASSBs from the micrometer to millimeter scale, which could benefit both battery quality inspection during ASSB fabrication and operation and the fundamental understanding of microstructure evolution/degradation during ASSB operation.

MICROSTRUCTURE OF SOLID-STATE ELECTROLYTE SEPARATOR

Like liquid-based batteries, ASSBs require a physical separator between the cathode and anode that is ionically conductive but electronically insulating to prevent short circuits. Ideally, a dense and durable SSE separator is strongly preferred to minimize ionic tortuosity and enhance microstructural integrity. The effects of the CIP process and electrochemical cycling on the microstructure of the separator were investigated. Cross-sectional views of the LPSCl separator layer in solid-state pouch cells at various stages are shown in Figure 3. Details of the segmentation, including color-washed sXCT slices, are provided in Figure S6. Additional top-down sXCT slices of the LPSCl separator are shown in Figure S5d-f.

Before CIP process, distinct edges of the LPSCl particles in the separator and darker regions, which represent pores, are clearly visible in the assembled cell, indicating that after the dry processing method,[33] the separator consists of clusters of loosely packed LPSCl particles bound together by fibrillated PTFE (Figure 3a). It should be noted that the PTFE fibril is not visible in sXCT images as the fibril diameter is below the sXCT resolution limit.[17] The particle distribution appears uniform across the image, with smaller particles spreading between larger ones, indicating effective particle dispersion during the dry fabrication process. A high LPSCl separator

https://doi.org/10.1021/acsenergylett.5c00956
ACS Energy Lett. 2025, 10, 3459−3470

homogeneity is critical for enhancing the density of the film in the subsequent isostatic pressing process.[34]

Following CIP process, the edges of the LPSCl particles become less distinct within the separator of the pressed cell (Figure 3b), and the microstructure is densified significantly. sXCT cross-section images of the cycled cell closely resemble that of the pressed sample (Figure 3c). This similarity is anticipated (and desired for a high-performing ASSB), as the separator does not actively participate in electrochemical reactions. The microstructure of the separator should remain intact during cycling unless parasitic microfractures develop due to mechanical stress, such as volume changes in the cathode or anode.

Leveraging the absorption contrast imaging mode, 3D models of the pores within the separator for the three samples (Figure 3d-f) derived from reconstruction and segmentation of the tomography data allow for quantitative evaluation of the differences in porosity and structure. The pore size distribution in the assembled cell ranges from 1.6 to 25.7 μm, while the pressed and cycled cells range from 1.6 to 13.5 μm, respectively. Besides, a decreased porosity is observed in the pressed (9.6 vol %) and cycled (10.4 vol %) cells than in the assembled cell (22.7 vol %) (Figure 3g). The model-estimated porosity of the pressurized LPSCl separator is consistent with our previous FIB-SEM[35] result. The lower porosity of the pressed cell indicates that more than half of the pores collapsed during the CIP process, and the microstructure remained stable during battery operation, as shown by the similar porosity of the cycled cell.

While CIP plays a crucial role in densifying the microstructure of the LPSCl separators, effectively reducing their porosity, the remaining ~10% porosity within the SSE separator still stands well above the ideal zero porosity target. Moving forward, strategies to advance more efficient densification (such as warm isostatic pressing at elevated temperature), SSE particle sizes optimization, and tailoring mechanical properties to enhance packing and minimize voids should be explored.

MICROSTRUCTURE OF COMPOSITE CATHODE

Due to the high modulus and sluggish ion diffusion in the oxide-based cathode material, SE and carbon additives are typically mixed with the cathode particles providing the ionic and electronic percolation, respectively. Thus, the microstructure of composite cathode electrodes, including porosity, particle distribution, tortuosity, and contact loss, plays a vital role in battery cycling performance. Ideally, a uniform distribution of particles—including cathode active material, SSE, carbon, and binder—is highly desirable. This ensures that each component is densified with minimal porosity while maintaining a well-connected percolating network, facilitating low tortuosity for efficient ion and electron transport. Thus, monitoring its evolution and stability offers valuable insight into fabrication process optimization and battery degradation mechanisms. Figure 4 shows the sXCT images, segmented 3D models, and quantitative analysis results of composite cathode electrode layers in the three pouch cell samples. The segmentation details showing the color-washed sXCT slices can be found in Figure S7. To validate the segmentation results of sXCT data, we carried out 3D FIB-SEM experiment and segmentation on the CIP-pressurized composite cathode (Figure S8). The detailed volume fraction of each component and discussion can be found in the Supporting Information to compare with that of pressed cathode extracted from sXCT data.

Cross-sectional (xy slice) sXCT images provide a detailed view of the composite cathode microstructure (Figure 4a-c). Differences in X-ray absorption enable the precise identification of its components: the bright spherical particles correspond to $LiNi_{0.8}Mn_{0.1}Co_{0.1}O_2$ (NMC811), the gray regions represent LPSCl, and the darkest areas denote the carbon binder domain (CBD), a mixture of pores, vapor-grown carbon fiber, and PTFE. The overlap in contrast between CBD and pores is due to the weak X-ray absorption by carbon, rendering CBD indistinguishable from pores under absorption contrast mode. The cross-section (xy) and top-down (xz) sXCT images in Figure S5 and the depth-wise volume fraction distribution in Figure S9 show a homogeneous mixture of NMC811, LPSCl, and pore/CBD across the thickness of composite cathodes. This well-integrated and consistent cathode composition can be attributed to the dry process, which facilitates fabrication of uniform and thick SSB electrode films.[17]

The composite cathode electrode had an initial thickness of 180 μm within the assembled cell, which decreased to approximately 130 μm after CIP process in both the pressed and cycled cells. Segmentation results show a noticeably smaller proportion of light red components (representing pores and CBD) than the assembled cell (Figure 4d) in the 3D models of the pressed (Figure 4e) and cycled samples (Figure 4f). Quantitative analysis of the segmented 3D models also highlights the decrease in porosity after CIP densification, with the pressed cathode showing 13.8 vol % porosity compared to 25.1 vol % in the assembled sample. After cycling, the porosity of composite cathode increased slightly to 15.6 vol % (Figure 4g). This could be attributed to the volume change and potentially particle cracks during the charge/discharge processes of NMC811, creating gaps/voids in the microstructure that lead to loss of physical contact,[2] higher tortuosity and charge transfer impedance,[30] and lower active material utilization.[36]

Following the CIP process, the porosity of the composite decreased, while the volume fractions of NMC811 and LPSCl increased—from 30.2 vol % to 36.3 vol % for NMC811 and from 44.6 vol % to 49.9 vol % for LPSCl. Despite these changes, the ratio of LPSCl to NMC811 remained consistent at approximately 1.4, similar to that observed in the assembled cell. However, after the cycling test, the volume fraction of LPSCl: NMC811 decreased to 1.1. The change may be due to partially irreversible volume changes in NMC811 after cycling or potential variations between cells.[36]

To investigate the ion transport pathway within the composite cathodes, tortuosity analysis on the segmented SSE phases in each composite cathode was performed using the open-source application TauFactor developed by Cooper et al.[37] Table 2 compares the tortuosity factor (τ) of SSE phase in each composite cathode across the thickness direction. The standard deviation of each tortuosity factor was calculated using the values obtained from representative volume (RV)

Table 2. Tortuosity Factor (τ) of Segmented LPSCl Phase in the Composite Cathode Electrode

Sample	Assembled	Pressed	Cycled
Tortuosity factor (τ)	2.79 ± 0.20	2.2 ± 0.05	2.49 ± 0.09

https://doi.org/10.1021/acsenergylett.5c00956
ACS Energy Lett. 2025, 10, 3459−3470

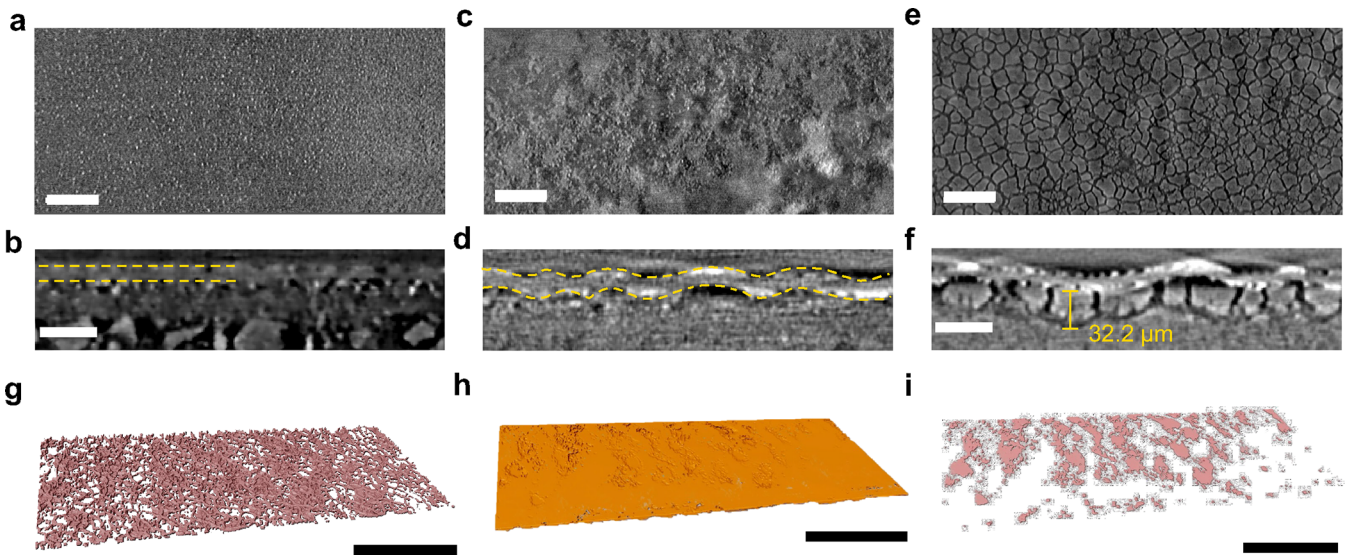

Figure 5. Morphology and microstructure of Si electrode. Top-down slice of Si electrode of (a) assembled, (b) pressed, and (c) cycled pouch cells. Scale bar: 150 μm. Cross-section slice of Si electrode of (d) assembled, (e) pressed, and (f) cycled pouch cells. Scale bar: 50 μm. 3D models of cycled pouch cell showing the (g) vertical fracture network in the Si electrode and (h) segmented Cu foil with dimples that match with (i) the interfacial fractures between Si and Cu. Scale bar: 400 μm.

analysis in the TauFactor application. It is worth noting that LPSCl exhibits >99.8% percolation in all three composite cathodes, indicating a uniform distribution and a well-connected network within the cathode. The SSE phase in the assembled cell showed the highest tortuosity factor of 2.79 and it decreased to 2.2 after CIP process. The lower tortuosity factor of the pressed cell enhances ion transport pathways, enabling more uniform ion movement, improved conductivity, and better Li diffusivity.[38,39] This can contribute to reduced overpotential, higher rate performance, and extended cycle life.[40,41] Comparing the tortuosity factor with the liquid-based LIBs, NMC cathode electrode typically results in a range of 1.3−3.0. Particularly, with a similar electrolyte phase volume fraction to the SSE phase reported in this work, the 40−50% porosity of the NMC cathode typically results in a tortuosity factor of 1.5−2.2, as determined through the 3D tomography-segmentation method.[42−44] After the cycling test, the tortuosity factor slightly increased to 2.49 in the cycled cell; this can be attributed to the higher porosity due to the void formation between the CAM and SSE that leads to more tortuous ionic pathways. The higher tortuosity in the cycled cell is consistent with the increased volume fraction of pore/CBD.

Another important parameter governing the ASSBs performance is the physical contact between the various composite components. Figure 4h compares the surface contact area of NMC811 particles within the composite cathode among the three samples. The active surface area (surface area of contact between the NMC811 and SSE) increased from 77.6 vol % (assembled) to 88.9 vol % (pressed) after CIP densification, yet later decreased to 83.3 vol % in the cycled cell. The growth of active surface area in the pressed cell shows that the applied isostatic pressure compressed the pores and facilitated better physical contact between CAM and SSE. This is imperative to maintain ionic transport and ensure better CAM utilization, namely higher reversible capacity. Meanwhile, the decline of active surface area in the cycled cell implies void formation, resulting from the volume change of NMC811 and plastic deformation of LPSCl. This rationale is based on the fact that CBD occupies a fixed volume and should stay constant during and after cycling. The increase of the CAM contact area to pores also aligns with the increase in pore/CBD volume in the cycled cell.

With the microstructures of cathode electrode extracted from sXCT results, one could correlate the structural information with the electrochemical performance. The higher volume fraction of pore/CBD and the decline of CAM active surface area resulted from loss of physical contact between the CAM and SSE. This could lead to polarization and reduced utilization, which could be observed after the C-rate test when the current density was restored back to C/10. The reversible capacity at C/10 after C-rate test was lower than the initial cycles, and a slight polarization could be observed from the dQ/dV plot (Figure S4b,c). Furthermore, the higher tortuosity observed in the cycled cell could also lead to lower effective ionic conductivity within the composite electrode, resulting in polarization (Figure S4b) and lower reversible capacity (Figure S4c) at higher current densities. Ideally, future experiments should focus on tracking the microstructure within the same cell *in situ* to better understand the nuances of this evolution, allowing for precise correlation quantitative analysis.

MICROSTRUCTURE OF Si ANODE

Silicon is one of most promising potential materials to be utilized as the next-generation anode due to its high theoretical capacity and low redox potential, elevating the energy density of the battery. While previous studies have shown its potential in ASSBs, the morphological evolution at the pouch cell scale remains unclear. sXCT of the Si at different stages of the process is analyzed to gain insightful information.

In the assembled cell, the Cu current collector (CC), approximately 13 μm thick, exhibits a flat morphology with Si particles uniformly distributed across its surface (Figure 5a). However, a noticeable gap at the μ-Si/LPSCl interface indicates poor contact between these components before applying 500 MPa fabrication pressure (Figure 5b).

https://doi.org/10.1021/acsenergylett.5c00956
ACS Energy Lett. 2025, 10, 3459−3470

After the CIP process, the gap between the Si anode and the LPSCl separator is reduced. However, the Cu CC morphology changed from flat to uneven (Figure 5c), exhibiting significant undulation as highlighted along the cross-section (Figure 5d). This pattern is also reflected in the separator morphology at the anode/separator interface but does not propagate past the LPSCl separator, leaving the cathode/separator interface a flat morphology. (Figure S5b). The undulation in the LPSCl separator closely mirrors that of the Cu CC, suggesting the nonuniform morphology of Cu CC may have plastically deformed the interfacial microstructure of LPSCl separator during CIP process. It is noted that after applying the fabrication pressure at 500 MPa, voids formed between the μ-Si/Cu interface, suggesting low adhesion between the Si and Cu CC without stack pressure. However, it is hypothesized that the gaps can be mitigated when under 5 MPa of stack pressure is applied.

Previous works have reported the columnar structures and mud-crack formation of the delithiated μSi anode within small-scale pellet-type cells.[6,45−47] Herein, we visualize the mud-crack networks and columnar structure nondestructively at millimeter scales in a pouch cell for the first time. The thickness of delithiated Si was in the range of 20−33 μm along the "wave" (Figure S5c), which was only 10−15 μm in the pristine state. The thickness change indicates the volume expansion during lithiation and remains partially lithiated due to the ICE of NMC811 and aligns with the porous structure reported in our previous work.[45] From the top-down sXCT image (Figure 5e), the mud crack network can be directly observed as having a darker contrast, with delithiated Si columns showing a slightly brighter contrast. Along the cross-section, the mud crack was observed to span vertically across the thickness of entire delithiated Si layer while showing a similar wavy pattern to Cu CC and separator (Figure 5f). We further investigate the amplitudes of waves in the pressed and cycled cells. Interestingly, the Cu CC in both samples shows similar amplitudes spreading vertically around 25−30 μm. Future studies will focus on the correlation between the mechanical properties of CC and the wavy structure after CIP process and during cycling.

Individual Si columns were labeled (Figure S10a) and visualized in 3D model (Figure S10b), revealing an average equivalent diameter of 29.6 ± 9.5 μm (Figure S10c). The 3D mud-crack structure is visualized in Figure 5g. Additionally, the area fraction of the mud-crack network (gaps between Si columns) was quantified from a segmented top-down slice covering 1.2 mm × 0.5 mm, yielding a value of 25.3 vol % (Figure S10d), which aligns closely with previously reported porosity values for delithiated Si.[45]

Beneath the mud-crack network, planar interfacial voids were observed at the Si/Cu CC interface. Figure 5h,i illustrates 3D models of the Cu CC and interfacial gaps, respectively, demonstrating that the dents on the Cu foil align with the interfacial voids. Quantitative analysis further deciphers that 40% of the Cu CC lost physical contact with delithiated Si, forming the interfacial voids as depicted in Figure 5i. These fractures indicate delamination between the Cu CC and Si, possibly due to low adhesion at the Si/Cu CC interface or the lack of stack pressure during the sXCT measurement. Delamination at the current collector-anode interface or between the anode and the SSE separator can result in nonuniform current distribution and state-of-charge, this could lead to polarization and hinder the electrochemical performance at higher current densities. Meanwhile, the intimate contact between the composite cathode and LPSCl separator that remained after the CIP process and cycling suggests a good adhesion, perhaps due to the presence of LPSCl in the composite cathode that facilitated the conformal contact and adhesion with LPSCl separator after CIP densification.

REALISTIC MODELING BASED ON sXCT RECONSTRUCTED 3D MODELS

To further explore the correlation between microstructure and electrochemical performance, significant efforts have been devoted to computational modeling of ASSB degradation. However, most prior models rely on stochastically generated geometries with nonrealistic particle arrangements. Hence, the modeling results might not reflect the true chemo-mechanical and structural degradation of ASSBs.

In contrast, the strength of synchrotron X-ray computed tomography lies in its ability to access and analyze the microstructure and morphology of ASSBs with exceptional detail. Throughout this work, we demonstrated how sXCT imaging and segmentation provide quantitative insights into critical microstructural information. Leveraging the non-destructive tomography characteristic, the 3D sXCT models at different states of charge or cycles can be integrated with computation modeling to understand the chemo-mechanical degradation mechanism of ASSBs.

sXCT-segmented 3D models provide true-to-life geometry and authentic microstructure representation, offering a practical starting point for advancing simulation and modeling. Figure 6 outlines a proposed multiphysics simulation workflow

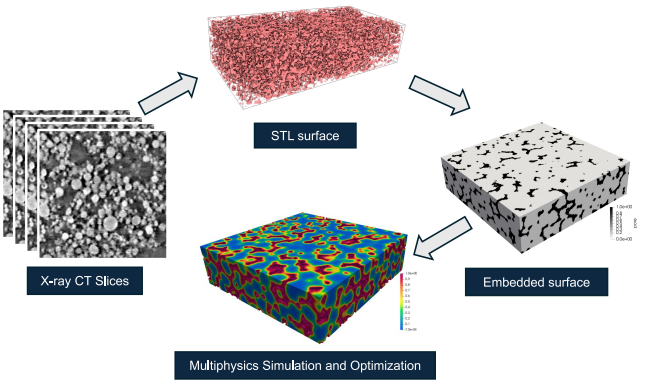

Figure 6. Multiphysics simulation workflow using realistic micro-XCT reconstructed 3D model. Schematic showing workflow of using real 3D XCT model for multiphysics simulation in four steps: obtaining sXCT slices, generating surface mesh file, regularizing noisy surface representations, and multiphysics simulation and optimization for ASSB degradation mechanism study. The colormaps in the simulation model contrast different phases representing particles, the void, and the regularized transition zone.

that incorporates sXCT-reconstructed 3D microstructures to study ASSB degradation mechanisms. The approach starts with reconstructing the measured sXCT slices to obtain realistic 3D models of ASSB microstructures. Subsequently, the surface representation of each segmented particle and features can be easily converted using commercially available software. However, a major challenge remains to regularize the particle surfaces to satisfy continuity and smoothness requirements in

https://doi.org/10.1021/acsenergylett.5c00956
ACS Energy Lett. 2025, 10, 3459−3470

numerical methods such as the finite element method. Our previously developed MOOSE (Multiphysics Object-Oriented Simulation Environment)-based application can regularize noisy surface representations.[48,49] The same application can then be used in conjunction with Cubit/Sculpt[50,51] to automatically generate a mesh of the cell with particle surfaces represented as side sets for subsequent finite element analysis. The particle surfaces and particle−particle interfaces play an important role in studying the effects of ASSB degradation mechanisms. Previous studies showed that loss of mechanical (and, therefore, electrochemical) contact between particle interfaces can lead to an abrupt decrease in capacity.[52−54]

Numerically discretizing the discontinuities across these interfaces renders another significant challenge. A variety of modeling/numerical approaches to represent such discontinuity have been explored within the Computational Mechanics community. These approaches fall into one of two categories: (1) sharp representations, such as the eXtended Finite Element Method (XFEM) and the Cohesive Zone Method (CZM), and (2) smooth/regularized representations, such as the Phase-Field Method (PFM). In particular, sharp representations of discontinuities allow for a straightforward application of interface conditions such as the traction-separation law for debonding and Butler−Volmer type electrochemical reactions. Moreover, sharp representations are generally more computationally efficient than regularized approaches, allowing for running a large batch of forward simulations during the design and optimization loop. It is worth noting that degradation mechanisms can also be incorporated into the interface conditions, and the sXCT-reconstructed microstructures allow for accurate representation of degradation sites with significant stress concentration, such as particle-void junctions and particle−particle delamination fronts, that are difficult (if not impossible) to be captured with synthetic computational domains or representative volume elements. The sXCT-reconstructed model naturally fits within the variational electro-chemo-thermo-mechanical framework for simulating charging−discharging cycles,[48] and the degradation mechanisms can be calibrated to predict an abrupt drop in capacity. Note that if otherwise a purely data-driven approach is used to predict such abrupt shift in the differential capacity (caused by a mechanism shift), a large amount of data will have to be collected to train a predictive model. In other words, the sXCT-based physics-based modeling approach can help alleviate the need for long-term data collection.

FUTURE DIRECTIONS

Although synchrotron micro-XCT provides an indispensable capability for investigating the microstructural evolution of ASSBs, particularly at the pouch cell level, several challenges remain that necessitate complementary characterization methods or further instrumental advancements to fully elucidate degradation and failure modes. Techniques such as FIB-SEM[55] and nano-XCT[56] can capture structural information at the nanoscale, enabling deeper and more precise quantitative analyses of microstructural changes. Additionally, microscopy and spectroscopy techniques capable of providing detailed chemical and structural insights—including X-ray fluorescence spectroscopy (XRF), scanning transmission X-ray microscopy (STXM),[40] and diffraction microscopy,[8,38] etc.—can offer complementary perspectives, enriching our understanding of microstructural evolution and degradation in ASSBs.

As for instrumental, due to the planar geometry of ASSB pouch cells, low-energy X-ray beams experience significant absorption or attenuation when the cell stack is aligned parallel to the beam, resulting in a long travel path through the entire cell. As a result, the X-ray signal becomes severely attenuated beyond certain rotation angles,[57] often leading to the formation of a missing wedge artifact. Although X-ray absorption can be mitigated by increasing the X-ray energy, the contrast of the lighter materials could become more difficult to differentiate. In contrast, computed laminography implements tilting the rotation axis along the beam direction before tomography. This modified sample geometry results in a more uniform X-ray penetration and cleaner images during sample rotation and mitigates loss of contrast derived from nonideal sample shapes. As a result, laminography enables scanning planar and high-absorbing samples while improving the imaging quality and mitigating the artifacts.[58]

For *operando* experiments, temporal resolution is always critical to the dynamic changes in batteries. With the higher brilliance/flux of the upgraded synchrotron radiation source, the imaging time is expected to be further reduced.[59] In addition to standard *operando* experiments, combining real-time reconstruction with dynamic 3D zooming (i.e., automatic lens change) facilitates high-resolution imaging of specific regions of interest.[25] Adopting this on-the-fly, multiscale imaging will significantly benefit the monitoring of dynamic changes in ASSBs. Future experiments will explore the integration of above-mentioned techniques to improve both the imaging quality and *operando* capability while shortening imaging time for probing the microstructure evolution of ASSB pouch cells.

Lastly, for sXCT data processing and analysis, the continuous advancement of synchrotron radiation sources and detectors is leading to a significant increase in tomography file sizes. Additionally, the accumulation of large tomography data sets in *operando* experiments presents challenges in efficient processing and analysis.[26,56,60] To address these issues, AI-assisted and deep-learning-based segmentation techniques are playing an increasingly critical role in accelerating data analysis and streamlining the entire workflow. Furthermore, deep-learning-based reconstruction and denoising methods have shown great potential in enhancing image quality and enabling high-throughput or low-dose imaging. These advancements are particularly beneficial for imaging beam-sensitive battery materials at lower X-ray energies and improving temporal resolution (fewer projections and/or shorter exposure time) for *operando* studies.[21,61,62]

sXCT offers quantitative insights into the ASSB microstructure, including (1) porosity of individual components, (2) particle size distribution, (3) volume fractions in the composite cathode, (4) contact surface areas between cathode active materials and either voids or solid electrolytes, and (5) delamination at the Cu current collector and Si anode interface.

https://doi.org/10.1021/acsenergylett.5c00956
ACS Energy Lett. 2025, 10, 3459−3470

Interface delamination, void formation, and cracking are well-known contributors to ASSB degradation. sXCT offers quantitative insights into the microstructure, including (1) porosity of individual components, (2) particle size distribution, (3) volume fractions in the composite cathode, (4) contact surface areas between cathode active materials and either voids or solid electrolytes, and (5) delamination at the Cu current collector and Si anode interface. By combining sXCT-deciphered microstructure with computational modeling based on realistic 3D-sXCT segmented models, we can gain a deeper understanding of the chemo-mechanical degradation processes in ASSBs.

sXCT investigation on ASSBs at the pouch cell level provides industry-relevant insights, aiding the design and engineering of solid-state batteries for practical applications.

Furthermore, sXCT investigation at the pouch cell level provides industry-relevant insights, aiding the design and engineering of solid-state batteries for practical applications. Future *in situ* and *operando* sXCT experiments on ASSB pouch cells with stack pressure applied will enable more correlative studies of microstructural evolution during extended cycling under conditions closer to real-world application. This work demonstrates that sXCT is an invaluable tool for probing microstructure and guiding the development of chemo-mechanically robust, high-performance electrodes for future all-solid-state batteries.

■ ASSOCIATED CONTENT

Supporting Information

The Supporting Information is available free of charge at https://pubs.acs.org/doi/10.1021/acsenergylett.5c00956.

Experimental section, sXCT beamline and reconstruction schematic, electrochemical data, ASSB pouch cell schematic, 3D FIB-SEM segmentation details, sXCT images, sXCT segmentation details, and segmentation details of cycled Si anode (PDF)

■ AUTHOR INFORMATION

Corresponding Author

Ying Shirley Meng − *Pritzker School of Molecular Engineering, University of Chicago, Chicago, Illinois 60637, United States; Aiiso Yufeng Li Family Department of NanoEngineering, University of California San Diego, La Jolla, California 92093, United States; Energy Storage Research Alliance, Argonne National Laboratory, Lemont, Illinois 60439, United States;* orcid.org/0000-0001-8936-8845; Email: shirleymeng@uchicago.edu, shirleymeng@anl.gov

Authors

Chen-Jui Huang − *Pritzker School of Molecular Engineering, University of Chicago, Chicago, Illinois 60637, United States; Advanced Photon Source, Argonne National Laboratory, Lemont, Illinois 60439, United States;* orcid.org/0000-0001-8338-1424

Jin An Sam Oh − *Aiiso Yufeng Li Family Department of NanoEngineering, University of California San Diego, La Jolla, California 92093, United States;* Present Address: Institute of Materials Research and Engineering (IMRE), Agency for Science, Technology and Research (A*STAR), Singapore 138634, Singapore; orcid.org/0000-0001-9336-234X

Marta Vicencio − *Aiiso Yufeng Li Family Department of NanoEngineering, University of California San Diego, La Jolla, California 92093, United States*

Tianchen Hu − *Argonne National Laboratory, Lemont, Illinois 60439, United States*

Hedi Yang − *Pritzker School of Molecular Engineering, University of Chicago, Chicago, Illinois 60637, United States*

James N. Burrow − *Pritzker School of Molecular Engineering, University of Chicago, Chicago, Illinois 60637, United States; Energy Storage Research Alliance, Argonne National Laboratory, Lemont, Illinois 60439, United States;* orcid.org/0000-0002-7445-3788

Yen-Fang Song − *National Synchrotron Radiation Research Center, Hsinchu 30076, Taiwan*

Gung-Chian Yin − *National Synchrotron Radiation Research Center, Hsinchu 30076, Taiwan*

Pavel Shevchenko − *Advanced Photon Source, Argonne National Laboratory, Lemont, Illinois 60439, United States*

Kamila M. Wiaderek − *Advanced Photon Source and Energy Storage Research Alliance, Argonne National Laboratory, Lemont, Illinois 60439, United States;* orcid.org/0000-0002-0051-3661

Bing Joe Hwang − *Sustainable Electrochemical Energy Development (SEED) Center, National Taiwan University of Science and Technology, Taipei 10607, Taiwan; National Synchrotron Radiation Research Center, Hsinchu 30076, Taiwan;* orcid.org/0000-0002-3873-2149

Complete contact information is available at: https://pubs.acs.org/10.1021/acsenergylett.5c00956

Author Contributions

C.-J.H. and Y.S.M. conceived the original idea and initiated the manuscript preparation. C.-J.H. developed the experimental plan with the help of J.A.S.O. C.-J.H., J.A.S.O., M.V., and H.Y. conducted the experiments. T.H. provided input on modeling. C.-J.H. performed sXCT measurements and analyzed the results with help from Y.-F.S. and G.-C.Y. P.S., K.M.W., and B.J.H. helped analyze the results. C.-J.H. and Y.S.M. co-led the manuscript preparation with inputs from all authors. The final version of the manuscript was approved by all authors.

Notes

The authors declare no competing financial interest.

Biographies

Chen-Jui Huang is a postdoctoral researcher at the Pritzker School of Molecular Engineering at University of Chicago and a resident associate at the Advanced Photon Source in Argonne National Laboratory. He received his Ph.D. in Chemical Engineering from the National Taiwan University of Science and Technology in 2021.

Jin An Sam Oh received his Ph.D. from the National University of Singapore and conducted postdoctoral research at the University of California, San Diego. He is currently a scientist at IMRE, A*STAR, specializing in the development and commercialization of all-solid-state battery technologies.

Marta Vicencio is a Ph.D. student in NanoEngineering with a concentration in Materials Science at the University of California, San Diego, working under the supervision of Professor Ying Shirley Meng.

https://doi.org/10.1021/acsenergylett.5c00956
ACS Energy Lett. 2025, 10, 3459−3470

Her research focuses on reducing stack pressure in high energy density anode materials for all-solid-state lithium-ion batteries.

Tianchen Hu is a core developer and maintainer of the Multiphysics simulation tool MOOSE, the MOOSE solid mechanics module, and several MOOSE-based applications for modeling fracture-related physics. Tianchen Hu is the author of the NEML2 library for GPGPU-accelerated high performance material modeling. He has extensive experience with energy storage systems.

Hedi Yang is a Ph.D. candidate at the Pritzker School of Molecular Engineering at University of Chicago with a focus on materials for sustainability under the supervision of Professor Ying Shirley Meng. His research focuses on the improvement and the commercialization of all-solid-state lithium-ion batteries.

James N. Burrow is the Deputy Assistant Director for the Energy Storage Research Alliance. He received his B.S. in Chemical Engineering from the University of Arkansas at Fayetteville; Ph.D. in Chemical Engineering from UT Austin; and was a postdoctoral scholar at UChicago and resident associate at the APS in Argonne National Laboratory.

Yen-Fang Song is the Research Scientist at National Synchrotron Radiation Research Center, serving as the spokesperson of TPS31A2 nano-Transmission X-ray Microscopy (nano-TXM) endstation. Her research fields of specialty are (1) microprojection X-ray microscopy (micro-PXM) and nano-TXM, (2) beamline optical design and development, (3) optical element analysis, and (4) X-ray absorption spectroscopy.

Gung-Chian Yin is the Division Head of Experimental facility Division at National Synchrotron Radiation Research Center, specializing in X-ray microscopy with over 20 years' experience, leading Transmission X-ray Microscopy, X-ray Nanoprobe, and tomography projects at Taiwan Light source and Taiwan Photon Source.

Pavel Shevchenko received his M.S. in biophysics from Moscow State University. He is currently a Senior Scientific Associate running 2-BM microtomography beamline as a part of imaging group (IMG), X-ray Science Division (XSD) at the Advanced Photon Source, Argonne National Laboratory.

Kamila M. Wiaderek is a chemist at Argonne's Advanced Photon Source, specializing in *operando* X-ray techniques to study battery materials. She leads the Electrochemistry Facility and serves as crosscut characterization lead for ESRA, advancing understanding of structure−property relationships in cathodes, anodes, and electrolytes.

Bing Joe Hwang is the Chair Professor of Chemical Engineering at National Taiwan University of Science and Technology. His research covers electrochemistry, spectroscopy, imaging, interfacial phenomena, materials science, and theoretical chemistry, facilitating understanding of electrochemical reaction mechanisms and enabling the discovery of promising materials for advanced batteries, fuel cells, and hydrogen production.

Ying Shirley Meng is a professor of Molecular Engineering at the Pritzker School of Molecular Engineering at University of Chicago. She serves as the Chief Scientist for Argonne Collaborative Center for Energy Storage Science (ACCESS) at Argonne National Laboratory and as the director of Energy Storage Research Alliance (ESRA).

■ ACKNOWLEDGMENTS

The authors would like to acknowledge Mr. Tsung-I Yeh for his help with sXCT measurement. The authors would like to thank Mr. Chien-Yu Lee, Dr. Bo-Yi Chen, Mr. Ying-Shuo Tseng, Mr. Shih-Ting Lo, and Dr. Hsiu-Chien Chan of NSRRC for their help at TPS 31A beamline sXCT (PXM) setup and image execution. This work is funded by the Joint Task Force Initiative (JTFI) at the Univeristy of Chicago (110007622) and LG Energy Solution through the Frontier Research Laboratory (FRL) program (100103332). Support for J.N.B., K.M.W., and Y.S.M. was provided by the Energy Storage Research Alliance "ESRA" (DE-AC02-06CH11357), an Energy Innovation Hub funded by the U.S. Department of Energy, Office of Science, Basic Energy Sciences.

■ REFERENCES

(1) Tan, D. H. S.; Meng, Y. S.; Jang, J. Scaling up high-energy-density sulfidic solid-state batteries: A lab-to-pilot perspective. *Joule* **2022**, *6* (8), 1755−1769.
(2) Janek, J.; Zeier, W. G. Challenges in speeding up solid-state battery development. *Nature Energy* **2023**, *8* (3), 230−240.
(3) Xiao, Y.; Wang, Y.; Bo, S.-H.; Kim, J. C.; Miara, L. J.; Ceder, G. Understanding interface stability in solid-state batteries. *Nature Reviews Materials* **2020**, *5* (2), 105−126.
(4) Banerjee, A.; Wang, X.; Fang, C.; Wu, E. A.; Meng, Y. S. Interfaces and Interphases in All-Solid-State Batteries with Inorganic Solid Electrolytes. *Chem. Rev.* **2020**, *120* (14), 6878−6933.
(5) Ham, S.-Y.; Yang, H.; Nunez-cuacuas, O.; Tan, D. H. S.; Chen, Y.-T.; Deysher, G.; Cronk, A.; Ridley, P.; Doux, J.-M.; Wu, E. A.; et al. Assessing the critical current density of all-solid-state Li metal symmetric and full cells. *Energy Storage Materials* **2023**, *55*, 455−462.
(6) Nelson, D. L.; Sandoval, S. E.; Pyo, J.; Bistri, D.; Thomas, T. A.; Cavallaro, K. A.; Lewis, J. A.; Iyer, A. S.; Shevchenko, P.; Di Leo, C. V.; et al. Fracture Dynamics in Silicon Anode Solid-State Batteries. *ACS Energy Lett.* **2024**, *9* (12), 6085−6095.
(7) Lewis, J. A.; Cortes, F. J. Q.; Liu, Y.; Miers, J. C.; Verma, A.; Vishnugopi, B. S.; Tippens, J.; Prakash, D.; Marchese, T. S.; Han, S. Y.; et al. Linking void and interphase evolution to electrochemistry in solid-state batteries using operando X-ray tomography. *Nat. Mater.* **2021**, *20* (4), 503−510.
(8) Ning, Z.; Jolly, D. S.; Li, G.; De Meyere, R.; Pu, S. D.; Chen, Y.; Kasemchainan, J.; Ihli, J.; Gong, C.; Liu, B.; et al. Visualizing plating-induced cracking in lithium-anode solid-electrolyte cells. *Nat. Mater.* **2021**, *20* (8), 1121−1129.
(9) Dixit, M. B.; Singh, N.; Horwath, J. P.; Shevchenko, P. D.; Jones, M.; Stach, E. A.; Arthur, T. S.; Hatzell, K. B. In Situ Investigation of Chemomechanical Effects in Thiophosphate Solid Electrolytes. *Matter* **2020**, *3* (6), 2138−2159.
(10) Zhang, M.; Chouchane, M.; Shojaee, S. A.; Winiarski, B.; Liu, Z.; Li, L.; Pelapur, R.; Shodiev, A.; Yao, W.; Doux, J.-M.; et al. Coupling of multiscale imaging analysis and computational modeling for understanding thick cathode degradation mechanisms. *Joule* **2023**, *7* (1), 201−220.
(11) Lu, B.; Li, W.; Cheng, D.; Bhamwala, B.; Ceja, M.; Bao, W.; Fang, C.; Meng, Y. S. Suppressing Chemical Corrosions of Lithium Metal Anodes. *Adv. Energy Mater.* **2022**, *12* (48), 2202012.
(12) Fang, C.; Lu, B.; Pawar, G.; Zhang, M.; Cheng, D.; Chen, S.; Ceja, M.; Doux, J.-M.; Musrock, H.; Cai, M.; et al. Pressure-tailored lithium deposition and dissolution in lithium metal batteries. *Nature Energy* **2021**, *6* (10), 987−994.
(13) Yang, Y.; Davies, D. M.; Yin, Y.; Borodin, O.; Lee, J. Z.; Fang, C.; Olguin, M.; Zhang, Y.; Sablina, E. S.; Wang, X.; et al. High-Efficiency Lithium-Metal Anode Enabled by Liquefied Gas Electrolytes. *Joule* **2019**, *3* (8), 1986−2000.
(14) Harrison, K. L.; Merrill, L. C.; Long, D. M.; Randolph, S. J.; Goriparti, S.; Christian, J.; Warren, B.; Roberts, S. A.; Harris, S. J.; Perry, D. L.; et al. Cryogenic electron microscopy reveals that applied pressure promotes short circuits in Li batteries. *iScience* **2021**, *24* (12), No. 103394.
(15) Burnett, T. L.; Kelley, R.; Winiarski, B.; Contreras, L.; Daly, M.; Gholinia, A.; Burke, M. G.; Withers, P. J. Large volume serial section

https://doi.org/10.1021/acsenergylett.5c00956
ACS Energy Lett. 2025, 10, 3459−3470

tomography by Xe Plasma FIB dual beam microscopy. *Ultramicroscopy* **2016**, *161*, 119−129.
(16) Lee, J. Z.; Wynn, T. A.; Schroeder, M. A.; Alvarado, J.; Wang, X.; Xu, K.; Meng, Y. S. Cryogenic Focused Ion Beam Characterization of Lithium Metal Anodes. *ACS Energy Letters* **2019**, *4* (2), 489−493.
(17) Yao, W.; Chouchane, M.; Li, W.; Bai, S.; Liu, Z.; Li, L.; Chen, A. X.; Sayahpour, B.; Shimizu, R.; Raghavendran, G.; et al. A 5 V-class cobalt-free battery cathode with high loading enabled by dry coating. *Energy Environ. Sci.* **2023**, *16* (4), 1620−1630.
(18) Rahe, C.; Kelly, S. T.; Rad, M. N.; Sauer, D. U.; Mayer, J.; Figgemeier, E. Nanoscale X-ray imaging of ageing in automotive lithium ion battery cells. *J. Power Sources* **2019**, *433*, 126631.
(19) Finegan, D. P.; Scheel, M.; Robinson, J. B.; Tjaden, B.; Di Michiel, M.; Hinds, G.; Brett, D. J.; Shearing, P. R. Investigating lithium-ion battery materials during overcharge-induced thermal runaway: an operando and multi-scale X-ray CT study. *Phys. Chem. Chem. Phys.* **2016**, *18* (45), 30912−30919.
(20) Yufit, V.; Tariq, F.; Eastwood, D. S.; Biton, M.; Wu, B.; Lee, P. D.; Brandon, N. P. Operando Visualization and Multi-scale Tomography Studies of Dendrite Formation and Dissolution in Zinc Batteries. *Joule* **2019**, *3* (2), 485−502.
(21) Scharf, J.; Chouchane, M.; Finegan, D. P.; Lu, B.; Redquest, C.; Kim, M. C.; Yao, W.; Franco, A. A.; Gostovic, D.; Liu, Z.; et al. Bridging nano- and microscale X-ray tomography for battery research by leveraging artificial intelligence. *Nat. Nanotechnol* **2022**, *17* (5), 446−459.
(22) Kastner, J.; Heinzl, C. X-Ray Tomography. In *Handbook of Advanced Non-Destructive Evaluation*; Ida, N., Meyendorf, N., Eds.; Springer International Publishing, 2018; pp 1−72.
(23) Naresh, K.; Khan, K. A.; Umer, R.; Cantwell, W. J. The use of X-ray computed tomography for design and process modeling of aerospace composites: A review. *Materials & Design* **2020**, *190*, No. 108553.
(24) Kastner, J.; Harrer, B.; Requena, G.; Brunke, O. A comparative study of high resolution cone beam X-ray tomography and synchrotron tomography applied to Fe- and Al-alloys. *NDT E Int.* **2010**, *43* (7−3), 599−605.
(25) Nikitin, V.; Tekawade, A.; Duchkov, A.; Shevchenko, P.; De Carlo, F. Real-time streaming tomographic reconstruction with on-demand data capturing and 3D zooming to regions of interest. *J. Synchrotron Radiat* **2022**, *29* (3), 816−828.
(26) Huang, Y.; Perlmutter, D.; Fei-Huei Su, A.; Quenum, J.; Shevchenko, P.; Parkinson, D. Y.; Zenyuk, I. V.; Ushizima, D. Detecting lithium plating dynamics in a solid-state battery with operando X-ray computed tomography using machine learning. *npj Computational Materials* **2023**, *9* (1), 93.
(27) Sakka, Y.; Matsumoto, M.; Yamashige, H.; Takeuchi, A.; Uesugi, M.; Uesugi, K.; Zhong, C.; Shimoda, K.; Okazaki, K. -i.; Orikasa, Y. Investigating Plastic Deformation Between Silicon and Solid Electrolyte in All-Solid-State Batteries Using Operando X-ray Tomography. *J. Electrochem. Soc.* **2024**, *171* (7), No. 070536.
(28) Kalnaus, S.; Dudney, N. J.; Westover, A. S.; Herbert, E.; Hackney, S. Solid-state batteries: The critical role of mechanics. *Science* **2023**, *381* (6664), No. eabg5998.
(29) Lee, Y.-G.; Fujiki, S.; Jung, C.; Suzuki, N.; Yashiro, N.; Omoda, R.; Ko, D.-S.; Shiratsuchi, T.; Sugimoto, T.; Ryu, S.; et al. High-energy long-cycling all-solid-state lithium metal batteries enabled by silver−carbon composite anodes. *Nature Energy* **2020**, *5* (4), 299−308.
(30) Chen, Y. T.; Jang, J.; Oh, J. A. S.; Ham, S. Y.; Yang, H.; Lee, D. J.; Vicencio, M.; Lee, J. B.; Tan, D. H. S.; Chouchane, M.; et al. Enabling Uniform and Accurate Control of Cycling Pressure for All-Solid-State Batteries. *Adv. Energy Mater.* **2024**, *14* (30), 2304327.
(31) Fath, J. P.; Alsheimer, L.; Storch, M.; Stadler, J.; Bandlow, J.; Hahn, S.; Riedel, R.; Wetzel, T. The influence of the anode overhang effect on the capacity of lithium-ion cells−a 0D-modeling approach. *Journal of Energy Storage* **2020**, *29*, No. 101344.
(32) O'Brien, A. I.; Trask, S. E.; Salpekar, D.; Son, S.-B.; Dunlop, A. R.; Veith, G. M.; Lu, W.; Ingram, B. J.; Abraham, D. P.; Jansen, A. N.; et al. Inactive Overhang in Silicon Anodes. *J. Electrochem. Soc.* **2024**, *171* (7), No. 070519.
(33) Lee, D. J.; Jang, J.; Lee, J. P.; Wu, J.; Chen, Y. T.; Holoubek, J.; Yu, K.; Ham, S. Y.; Jeon, Y.; Kim, T. H.; et al. Physio-Electrochemically Durable Dry-Processed Solid-State Electrolyte Films for All-Solid-State Batteries. *Adv. Funct. Mater.* **2023**, *33* (28), 2301341.
(34) Dixit, M.; Beamer, C.; Amin, R.; Shipley, J.; Eklund, R.; Muralidharan, N.; Lindqvist, L.; Fritz, A.; Essehli, R.; Balasubramanian, M.; et al. The Role of Isostatic Pressing in Large-Scale Production of Solid-State Batteries. *ACS Energy Letters* **2022**, *7* (11), 3936−3946.
(35) Cronk, A.; Chen, Y.-T.; Deysher, G.; Ham, S.-Y.; Yang, H.; Ridley, P.; Sayahpour, B.; Nguyen, L. H. B.; Oh, J. A. S.; Jang, J.; et al. Overcoming the Interfacial Challenges of LiFePO4 in Inorganic All-Solid-State Batteries. *ACS Energy Letters* **2023**, *8* (1), 827−835.
(36) Koerver, R.; Zhang, W.; de Biasi, L.; Schweidler, S.; Kondrakov, A. O.; Kolling, S.; Brezesinski, T.; Hartmann, P.; Zeier, W. G.; Janek, J. Chemo-mechanical expansion of lithium electrode materials−on the route to mechanically optimized all-solid-state batteries. *Energy Environ. Sci.* **2018**, *11* (8), 2142−2158.
(37) Cooper, S. J.; Bertei, A.; Shearing, P. R.; Kilner, J. A.; Brandon, N. P. TauFactor: An open-source application for calculating tortuosity factors from tomographic data. *SoftwareX* **2016**, *5*, 203−210.
(38) Stavola, A. M.; Sun, X.; Guida, D. P.; Bruck, A. M.; Cao, D.; Okasinski, J. S.; Chuang, A. C.; Zhu, H.; Gallaway, J. W. Lithiation Gradients and Tortuosity Factors in Thick NMC111-Argyrodite Solid-State Cathodes. *ACS Energy Lett.* **2023**, *8* (2), 1273−1280.
(39) Froboese, L.; Sichel, J. F. v. d.; Loellhoeffel, T.; Helmers, L.; Kwade, A. Effect of Microstructure on the Ionic Conductivity of an All Solid-State Battery Electrode. *J. Electrochem. Soc.* **2019**, *166* (2), A318−A328.
(40) Liu, Q. S.; An, H. W.; Wang, X. F.; Kong, F. P.; Sun, Y. C.; Gong, Y. X.; Lou, S. F.; Shi, Y. F.; Sun, N.; Deng, B.; et al. Effective transport network driven by tortuosity gradient enables high-electrochem-active solid-state batteries. *Natl. Sci. Rev.* **2023**, *10* (3), No. nwac272.
(41) Hlushkou, D.; Reising, A. E.; Kaiser, N.; Spannenberger, S.; Schlabach, S.; Kato, Y.; Roling, B.; Tallarek, U. The influence of void space on ion transport in a composite cathode for all-solid-state batteries. *J. Power Sources* **2018**, *396*, 363−370.
(42) Landesfeind, J.; Ebner, M.; Eldiven, A.; Wood, V.; Gasteiger, H. A. Tortuosity of Battery Electrodes: Validation of Impedance-Derived Values and Critical Comparison with 3D Tomography. *J. Electrochem. Soc.* **2018**, *165* (3), A469−A476.
(43) Ebner, M.; Chung, D. W.; García, R. E.; Wood, V. Tortuosity Anisotropy in Lithium-Ion Battery Electrodes. *Adv. Energy Mater.* **2014**, *4* (5), 1301278.
(44) Usseglio-Viretta, F. L. E.; Colclasure, A.; Mistry, A. N.; Claver, K. P. Y.; Pouraghajan, F.; Finegan, D. P.; Heenan, T. M. M.; Abraham, D.; Mukherjee, P. P.; Wheeler, D.; et al. Resolving the Discrepancy in Tortuosity Factor Estimation for Li-Ion Battery Electrodes through Micro-Macro Modeling and Experiment. *J. Electrochem. Soc.* **2018**, *165* (14), A3403−A3426.
(45) Tan, D. H. S.; Chen, Y. T.; Yang, H.; Bao, W.; Sreenarayanan, B.; Doux, J. M.; Li, W.; Lu, B.; Ham, S. Y.; Sayahpour, B.; et al. Carbon-free high-loading silicon anodes enabled by sulfide solid electrolytes. *Science* **2021**, *373* (6562), 1494−1499.
(46) Cao, Q.; Sun, Z.-T.; Ye, K.; Shen, P.; Jiang, K.; Bo, S.-H. Stacking pressure homogenizes the electrochemical lithiation reaction of silicon anode in solid-state batteries. *Energy Storage Materials* **2024**, *67*, No. 103246.
(47) Huo, H.; Jiang, M.; Bai, Y.; Ahmed, S.; Volz, K.; Hartmann, H.; Henss, A.; Singh, C. V.; Raabe, D.; Janek, J. Chemo-mechanical failure mechanisms of the silicon anode in solid-state batteries. *Nat. Mater.* **2024**, *23* (4), 543−551.
(48) Hu, T.; Messner, M. C.; Barai, P.; Barua, B. A Three-Dimensional, Thermodynamically and Variationally Consistent, Fully

Coupled, Electro-Chemo-Thermo-Mechanical Model of Solid-State Batteries. *J. Electrochem. Soc.* **2023**, *170* (12), 123501.
(49) Giudicelli, G.; Lindsay, A.; Harbour, L.; Icenhour, C.; Li, M.; Hansel, J. E.; German, P.; Behne, P.; Marin, O.; Stogner, R. H.; et al. 3.0 - MOOSE: Enabling massively parallel multiphysics simulations. *SoftwareX* **2024**, *26*, 101690.
(50) Owen, S. J. Sculpt: A new tool for automatic parallel hex meshing. Proposed for presentation at the *1500 External Review*; USDOE, Albuquerque, NM, USA, 2013.
(51) Owen, S. J.; Shelton, T. R. Evaluation of grid-based hex meshes for solid mechanics. *Engineering with Computers* **2015**, *31* (3), 529−543.
(52) Pietsch, P.; Westhoff, D.; Feinauer, J.; Eller, J.; Marone, F.; Stampanoni, M.; Schmidt, V.; Wood, V. Quantifying microstructural dynamics and electrochemical activity of graphite and silicon-graphite lithium ion battery anodes. *Nat. Commun.* **2016**, *7*, 12909.
(53) Kong, L.; Tang, C.; Peng, H. J.; Huang, J. Q.; Zhang, Q. Advanced energy materials for flexible batteries in energy storage: A review. *SmartMat* **2020**, *1* (1), 1−35.
(54) Tan, D. H. S.; Banerjee, A.; Chen, Z.; Meng, Y. S. From nanoscale interface characterization to sustainable energy storage using all-solid-state batteries. *Nat. Nanotechnol* **2020**, *15* (3), 170−180.
(55) Hong, S.-B.; Lee, Y.-J.; Kim, U.-H.; Bak, C.; Lee, Y. M.; Cho, W.; Hah, H. J.; Sun, Y.-K.; Kim, D.-W. All-Solid-State Lithium Batteries: Li+-Conducting Ionomer Binder for Dry-Processed Composite Cathodes. *ACS Energy Letters* **2022**, *7* (3), 1092−1100.
(56) Su, Z.; Decencière, E.; Nguyen, T.-T.; El-Amiry, K.; De Andrade, V.; Franco, A. A.; Demortière, A. Artificial neural network approach for multiphase segmentation of battery electrode nano-CT images. *npj Computational Materials* **2022**, *8* (1), 30.
(57) X-Ray Tomography. In *X-ray Microscopy*; Jacobsen, C., Ed.; Advances in Microscopy and Microanalysis; Cambridge University Press, 2019; pp 321−349.
(58) Nikitin, V.; Wildenberg, G.; Mittone, A.; Shevchenko, P.; Deriy, A.; De Carlo, F. Laminography as a tool for imaging large-size samples with high resolution. *J. Synchrotron Radiat* **2024**, *31* (4), 851−866.
(59) Kerby, J. The Advanced Photon Source Upgrade: A Brighter Future for X-Ray Science. *Synchrotron Radiation News* **2023**, *36* (4), 26−27.
(60) Muller, S.; Sauter, C.; Shunmugasundaram, R.; Wenzler, N.; De Andrade, V.; De Carlo, F.; Konukoglu, E.; Wood, V. Deep learning-based segmentation of lithium-ion battery microstructures enhanced by artificially generated electrodes. *Nat. Commun.* **2021**, *12* (1), 6205.
(61) Liu, Z.; Bicer, T.; Kettimuthu, R.; Gursoy, D.; De Carlo, F.; Foster, I. TomoGAN: low-dose synchrotron x-ray tomography with generative adversarial networks: discussion. *J. Opt Soc. Am. A Opt Image Sci. Vis* **2020**, *37* (3), 422−434.
(62) Zhang, J.; Lee, W.-K.; Ge, M. Sub-10 second fly-scan nano-tomography using machine learning. *Communications Materials* **2022**, *3* (1), 91.

https://doi.org/10.1021/acsenergylett.5c00956
ACS Energy Lett. 2025, 10, 3459−3470